NANO · MICRO small
www.small-journal.com

A Novel Biosensor Based on Molybdenum Disulfide (MoS_2) Modified Porous Anodic Aluminum Oxide Nanochannels for Ultrasensitive microRNA-155 Detection

Songlong Jiao, Lei Liu, Jianqiao Wang, Kejian Ma, and Jun Lv*

Artificial photoresponsive nanochannels have attracted widespread attention because of their capacity to achieve ion transport through light modulation. Herein, a biosensor for ultrasensitive miRNA-155 detection is devised based on molybdenum disulfide (MoS_2) modified porous anodic aluminum oxide (AAO) photoresponsive nanochannels by atomic layer deposition (ALD). According to the optimized experimental results, when the cycles of ALD, the wavelength, and the power of the excitation laser are 70 cycles, 450 nm, and 80 mW, respectively, the most supreme photocurrent performance of these photoresponsive nanochannels are obtained. AAO nanochannels modified with MoS_2 can work as a photoelectrochemical (PEC) biosensor by generating photoexcitation current; what is more, the high channel density in AAO can magnify the ion current signal response effectively by aggrandizing the flux of electroactive species. By using AAO photoresponsive nanochannels with an average diameter of 150 nm as PEC biosensor, an ultrasensitive detection record ranging from 0.01 fM to 0.01 nM with a detection limit of 3 aM can be achieved. This work not only proposes a simple method for manufacturing semiconductor photoresponsive nanochannels, but also exhibits great potential in the ultrasensitive detection of biomolecules.

1. Introduction

Over the past decades, biological nanochannel has sprung up in the fields of chemistry,[1] material,[2] and biology,[3] and attracted wide attention in the battery,[4] ionic transport,[5] genetic engineering,[6] genomes sequencing,[7] chemical analysis,[8] and biosensing applications.[9] Inspired by green chlorophyll pigments capturing solar energy to actualize electron transport in plant thylakoid membranes, artificial photoresponsive nanochannels whose ion-transport capabilities can be precisely controlled by the photoelectric conversion effect may play a greater role in ultrasensitive detection.[10,11] The current strategy to construct artificial photoresponsive nanochannels is generally to qualify artificial proteins or solid-state ion nanochannels with photoresponsive molecules, such as hydroxypyrene, azobenzene, and spiropyran.[12,13] However, semiconductors as optoelectronic materials modified nanochannels have rarely been reported due to the complexity of preparation and the tendency to clog up nanochannels, although they are more stable. Among the various solid-state nanochannels, including silicon nitride,[14] glass,[15] quartz,[16] anodic aluminum oxide (AAO),[17] graphene,[18] and organic polymers (such as polyethylene terephthalate and polyimide),[19,20] AAO membrane possesses significant advantages because of its uniform nanochannels size, adjustable pore density, and excellent stability for photoresponsive applications.[21]

Appropriate physical or chemical modification for AAO can improve the performance in photoresponsive applications. As an example, MoS_2 possessed excellent light absorption coefficient and long photoexcited carrier lifetimes can work as a perfect semiconductor optoelectronic material for photoresponsive nanochannels.[22,23] Recently, the precise growth of MoS_2 films using atomic layer deposition (ALD) by chemical sorption and self-limiting chemical reactions provides potential effective means for controllable modification,[24,25] which offers a possibility to deposit MoS_2 films on AAO with ultrahigh aspect ratios as photoresponsive nanochannel. Theoretically, for photoresponsive nanochannel, it can be used as a photoelectrochemical (PEC) biosensor to generate photoexcitation current,[26–28] what is more, the AAO nanochannels have an ion-transmitting current response, and accordingly could considerably enhance the detection sensitivity. Although many PEC biosensors have been constructed based on various photosensitive materials,[29,30] the strategy by altering the PEC device to design the biosensor has not been reported yet.

In this work, the photoresponsive nanochannel was fabricated by using ALD to deposit MoS_2 films on the surface and inside the channel of AAO. The effects of AAO with different apertures, different numbers of ALD cycles, together with the wavelength and power of the excitation laser on the photocurrent performance of photoresponsive nanochannel were studied, and the relevant detection sensitivity and mechanism for miRNA-155 were under discussion.

S. Jiao, Prof. L. Liu, J. Wang, K. Ma, J. Lv
Jiangsu Key Laboratory for Design and Manufacture of Micro-Nano Biomedical Instruments, School of Mechanical Engineering
Southeast University
Nanjing 211189, China
E-mail: liulei@seu.edu.cn

The ORCID identification number(s) for the author(s) of this article can be found under https://doi.org/10.1002/smll.202001223.

DOI: 10.1002/smll.202001223

2. Results and Discussion

2.1. Fabrication and Morphology of Photoresponsive Nanochannels

As a simple and stable method to grow conformal and uniform films, ALD was used to deposit MoS_2 films on the AAO substrate. **Figure 1**A shows the ALD of MoS_2 on four AAO substrates, with diameters of about 90, 130, 180, and 250 nm, respectively (named as AAO-100, AAO-150, AAO-200, and AAO-250, respectively). In the ALD process, the gaseous precursors enable MoS_2 grow on the wall and the upper surface of the AAO nanochannel (Figure 1B). In appearance, the original translucent and gray-white AAO substrate becomes dark after ALD (Figure 1C), which is covered by MoS_2 films. The thickness of the whole AAO is estimated to be about 95 µm from Figure 1D, the neat and regular AAO nanochannel ensure the ion transport in the later experiments. The MoS_2 films with controllable thickness obtained by 10, 20, 30, 50, 70, and 90 ALD cycles on AAO substrates are denoted as 10-MoS_2/AAO, 30-MoS_2/AAO, 50-MoS_2/AAO, 70-MoS_2/AAO, and 90-MoS_2/AAO, respectively.

The surface of pristine AAO-150 is smooth, and its nanochannels diameter is about 151.92 nm (Figure 1E). After 10 ALD cycles, small crystallites or particles appear, and the MoS_2 films seem to be discontinuous (Figure 1F). For 50-MoS_2/AAO-150 (Figure 1G), the excess flake-like MoS_2 becomes more pronounced, and the apparent grain size has a significant increase. When the ALD cycles increased to 90, the diameter of the AAO nanochannel was reduced by 38.44% (Figure 1H). As the number of ALD cycles increases, the nanochannels of AAO become more out-of-round, because MoS_2 is more natural to grow in the hole wall with large curvature during the ALD process. The SEM images of different cycles MoS_2 grown on AAO with other nanochannel diameters are shown in Figure S1, Supporting Information, and their growth conditions are similar to AAO-150. For AAO-100 with the smallest nanochannels diameter, when the cycles number is 90, the nanochannels are entirely covered by MoS_2 nanoflakes (Figure S2, Supporting Information).

From the top view of TEM images of 10-ALD-cycles MoS_2 on AAO with 150 nm nanochannels (Figure 1I,J), the striations of layered MoS_2 with the 0.65 nm spacing of (002) planes indicate that MoS_2 flakes grow perpendicular to the surface flat of AAO.[31] Layered MoS_2 films are also successfully grown on the inner wall of the AAO nanochannel, as illustrated in Figure 1K,L. Owing to the optoelectronic semiconductor properties of MoS_2, the more ALD cycles of MoS_2 will bring about higher the photocurrent intensity but also shrink the nanochannel size, which goes against ion transport. Therefore, there is an optimal number of ALD cycles in order to balance photoelectric performance and ion transmission. It can be seen from **Figure 2**A that the AAO nanochannels diameters decrease linearly as the number of ALD cycles increases. Therefore, the effect of nanochannel shrinkage can be regulated by ALD, and the size of the nanochannels can be precisely controlled.

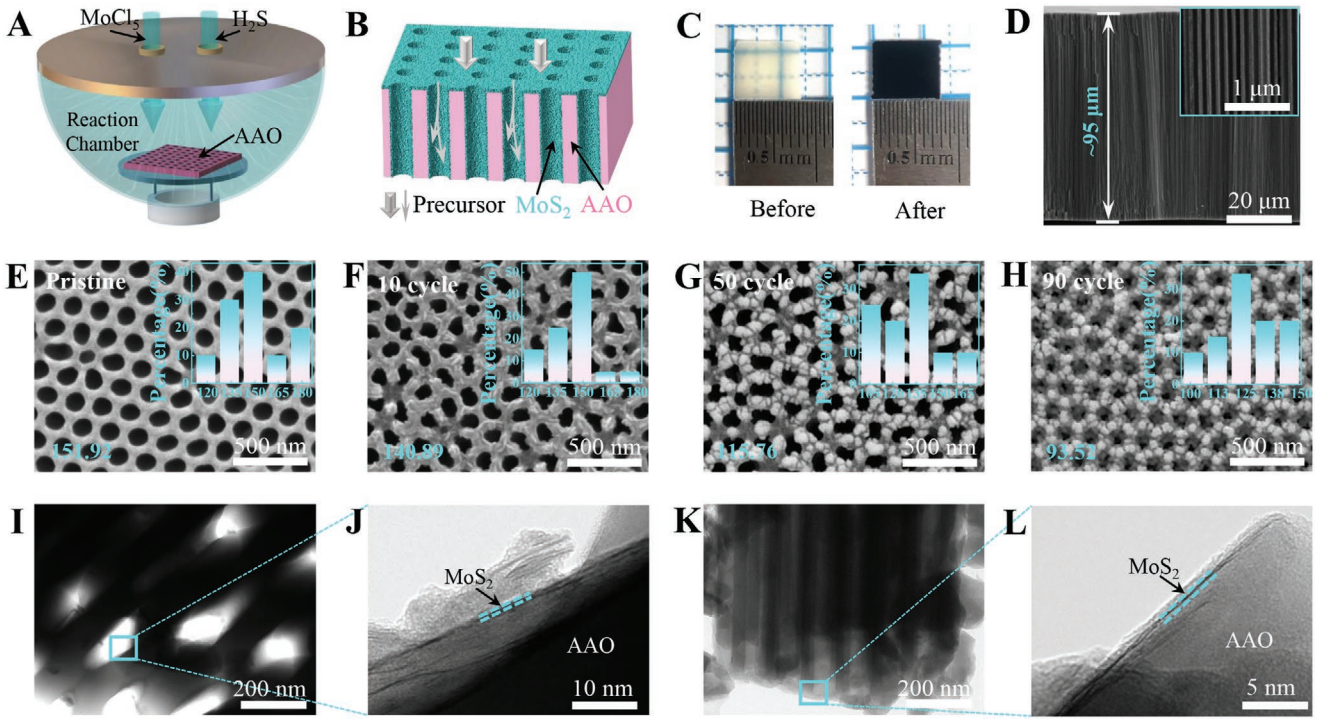

Figure 1. A) Schematic showing the ALD of MoS_2. B) Optical photographs of the AAO (left) and the 50-ALD-cycles MoS_2 films on AAO (right). C) Schematic illustration of MoS_2/AAO photoresponsive nanochannel. D) SEM images of the side view of AAO-150. E–H) SEM images of MoS_2 films grown on AAO-150 by 0, 10, 50, and 90 cycles, respectively; the histogram representing the diameter of the AAO nanochannels after ALD of MoS_2. TEM images of I,J) the top view and K,L) the side view of 10-MoS_2/AAO-150 photoresponsive nanochannel.

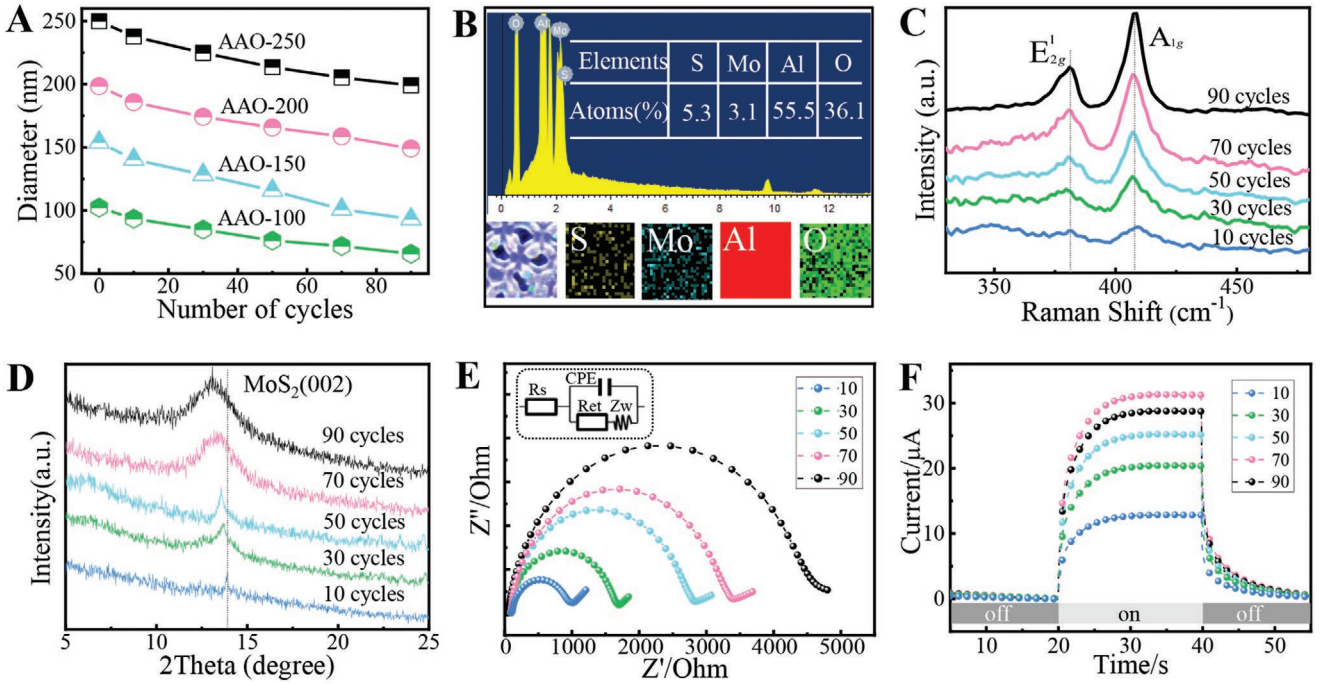

Figure 2. A) The change of AAO apertures with different numbers of ALD cycles. B) EDS spectrum and elemental mapping profiles of 10-MoS_2/AAO-150. C) Raman spectra, D) XRD, E) EIS, and F) Photocurrent of different cycles of MoS_2 on AAO-150. The schematic of the equivalent circuit (inset in (E)) consisted of solution resistance (Rs), electron-transfer resistance (Ret), constant-phase element (CPE), and Warburg impedance (Zw).

2.2. Component Characterization of the Photoresponsive Nanochannels

The sample is characterized by energy-dispersive X-ray spectroscopy (EDS) (Figure 2B), confirming that S and Mo are distributed on the surface of AAO and the atomic percentage of Mo and S are 3.1% and 5.3%, respectively. The ratio of Mo/S is greater than 1/2 indicating MoS_2 has S defects. In the Raman spectra (Figure 2C), the locations of the peaks located at 380 and 406 cm^{-1} correspond to E^1_{2g} and A_{1g} vibrational modes.[32] According to the X-ray diffraction (XRD) pattern in Figure 2D, an obvious diffraction peak can be observed at about 14.4°, corresponding to the (002) planes of 2H-MoS_2 (JPCDS card no. 37–1492).[33] This peak shifts to a lower angle with increasing the ALD cycles, which is due to the expansion of interlayer spacing.[34] AAO is composed of nanochannels with large curvatures and rough inner walls, which is different from the flat substrate (such as silicon wafer or oxide silicon wafer).[35] The growth of MoS_2 by ALD on AAO inner walls will not one layer by one layer in a large area by an ideal way, and defects/dislocations may appear which result in the expansion of the interlayer distance with the increase of the number of ALD cycles. In addition, TEM images shown in Figure S3, Supporting Information, provide direct evidence for this deduction.

In Figure 2E, electrochemical impedance spectroscopy (EIS) is used as an effective method for characterizing the interface properties of different cycles of MoS_2/AAO-150 electrodes. The electron transfer impedance (Ret), equal to the diameter of a semicircle,[36] reflects the diffusion limit of MoS_2/AAO and the solution during the electron transfer process. Ret increases as the number of cycle increases since more MoS_2 with poor semiconductor conductivity deposited on AAO. Figure 2F shows the photocurrent intensity of MoS_2/AAO-150 for different ALD cycles. When the number of cycles is 70, the photocurrent intensity of the photoresponsive nanochannel reaches the maximum. As an optoelectronic semiconductor, MoS_2 generates a photogenerated current under laser irradiation, and also affects electron transmission due to poor conductivity. The electronic transport performance of MoS_2 deteriorate along with the increase of MoS_2 layers. However, only exterior MoS_2 can receive photon energy, which leads to an increase in the photogenerated electrons and then stabilize (Figure S4, Supporting Information). Therefore, the photocurrent increases first and then decreases with the number of ALD-MoS_2 cycles. 70 cycles of MoS_2 are used to modify AAO in this work unless otherwise specified.

2.3. Fabrication of Biosensing Device

A brand new detection device was developed based on PEC biosensor, a thriving technology having specific bioaffinity characteristics and inherent sensitivity, using MoS_2/AAO photoresponsive nanochannels. The device is used to detect MicroRNA-155 (miRNA-155), which is considered as a biomarker in the diagnosis and prognosis of cancer, such as breast cancer. **Figure 3**A shows the construction process of the biosensor electrode. After the preparation of MoS_2/AAO nanochannel, the AuNPs was deposited on MoS_2/AAO (Figure S5, Supporting Information) to enhance the photoelectron generation capability of the MoS_2 films and immobilize SH-modified probe RNA onto the AuNPs/MoS_2/AAO electrode via the Au-S bond. The AuNPs are adsorbed on MoS_2 flakes by

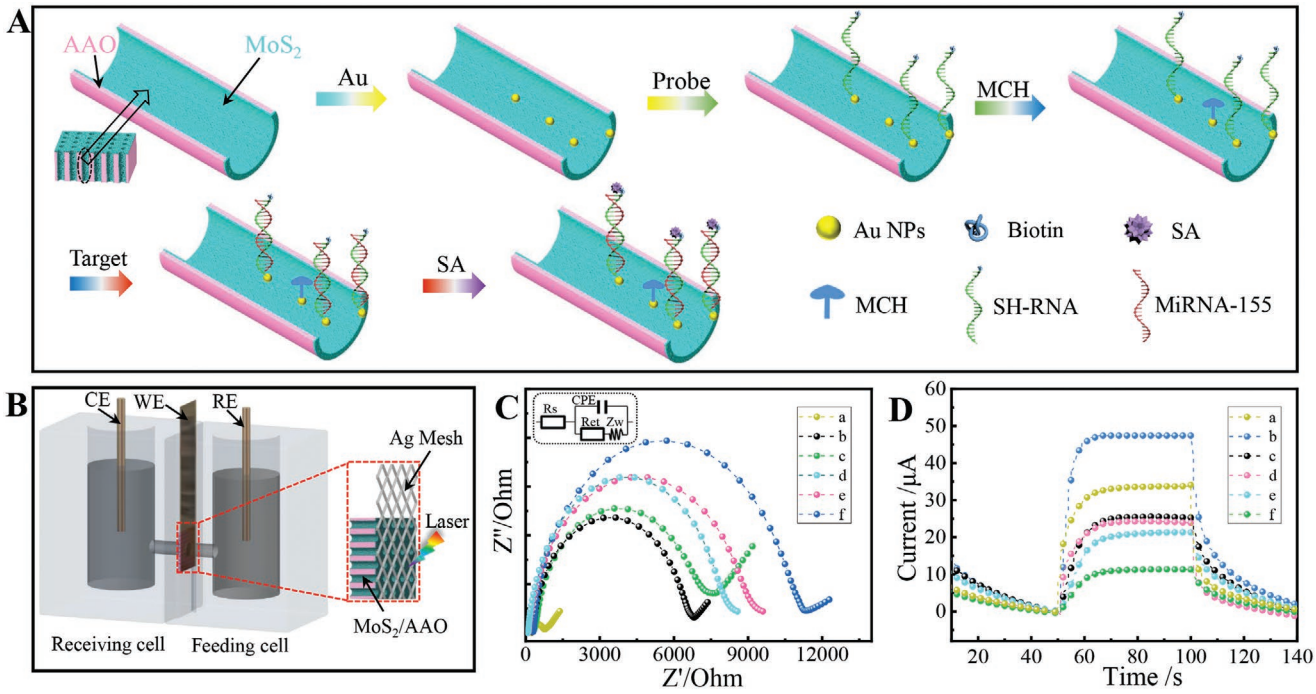

Figure 3. A) Fabrication procedures of miRNA detection principle. B) Schematic illustration of a PEC biosensor based on MoS_2/AAO photoresponsive nanochannel. Ag mesh connected to MoS_2/AAO as working electrode (WE), a saturated calomel electrode as reference electrode (RE), and a platinum wire as counter electrode (CE). C) EIS and D) Photocurrent of (a) MoS_2/AAO, (b) AuNPs/MoS_2/AAO, (c) SH-RNA/AuNPs/MoS_2/AAO, (d) MCH/SH-RNA/AuNPs/MoS_2/AAO, (e) MiRNA/MCH/SH-RNA/AuNPs/70-MoS_2/AAO-150, (f) SA/miRNA/MCH/SH-RNA/AuNPs/70-MoS_2/AAO-150.

weak van der Waals, and mostly located on the top site directly above S atom.[37,38] As shown in Figure S6, Supporting Information, The CV curve repeated 20 times coincides very well, which shows that the combination of AuNPs and MoS_2 is very stable during the electrochemical test. The excellent interaction between AuNPs and MoS_2 is conducive to improving the detection performance of the biosensor. Then, 20 µL biotin-labelled SH-RNA solutions was added to the AuNPs/MoS_2/AAO electrode by dripping, and incubated at 25 °C for 12 h. After the cultivation, the SH-RNA not connected by the Au—S bond was washed away three times with the washing buffer. MiRNA-155 solutions of different concentrations were dropped on the surface of the electrode, placed on a shaking table, and cultured for 2 h. Then, the non-hybridized miRNA-155 was washed off with 1 × SSC rinse, that is, the miRNA/SH-RNA/AuNPs/MoS_2/AAO electrode was prepared. The electrode was sealed with a solution (10 mM) of 20 µL MCH to occupy the unreacted position points to prevent the generation of false-positive signals. Then, 20 L 15 µg mL^{-1} of streptavidin (SA) was dripped onto the surface of the electrode and reacted at room temperature for 30 min. After that, the unconnected SA was rinsed several times with the buffer to remove the unconnected SA to obtain SA/miRNA/SH-RNA/AuNPs/MoS_2/AAO electrode.

The home-made biosensor based on "U"-type separation device was adopted as the miRNA-155 detection platform (Figure 3B). The device employs silver mesh with large porosity (>85%) as the working electrode connected to MoS_2/AAO. The silver mesh ensures that it will not block the nanochannels to affect the ion transmission through the channels. The biomolecules based on miRNA-155 in nanochannels can hinder ion transport and in turn affect current changes. Compared with conventional PEC biosensors, different amounts of miRNA-155 not only affect the photoexcitation current but also the ion-transport current from feeding cell to receiving cell. Therefore, the device using the current as the detection signal of different concentrations of miRNA can enhance the detection sensitivity.

Figure 3C is the EIS corresponding to different modification steps of the electrode, and the inserted illustration is an equivalent circuit diagram. The resistance value (curve a) of the MoS_2/AAO is relatively small. After the AuNPs are modified, the resistance value decreases (curve b) due to the excellent electrical conductivity of AuNPs. After modification of SH-RNA, MCH, miRNA, and SA, the resistance correspondingly increases due to the weak conductivity of the molecules (curves c, d, e, and f), indicating that the electron transport resistances are very high and the electrodes are difficult to exchange electrons with solution. The PEC test was conducted in 0.1 M PBS (pH = 7.4) solution containing 0.1 M AA and 0.1 M KCl with a laser of 450 nm and a voltage of 0.1 V. As shown in Figure 3D, curve a shows that the AAO modified with MoS_2 has a strong current, indicating that MoS_2 is an excellent photoelectric conversion material. The current of AuNPs modified MoS_2/AAO has a strong increase (curve b), which is mainly due to the fact that the generation of Au/MoS_2 schottky junction increases the separation efficiency of electron–hole and prolongs the recombination time of electron–hole pairs. The attenuation of SH-RNA/Au/MoS_2/AAO current (curve c) may be attributed to the following aspects. First, the Au/MoS_2/AAO captures SH-RNA through the Au—S bond, producing a spatial effect that impedes the electron donor diffusion on the electrode surface and improves

the efficiency of the electron-hole pair recombination in MoS_2. Second, there is an electrostatic repulsion between negatively charged SH-RNA and AA. Because the AA is electronegative in pH = 7.4 solution, the negative charge of SH-RNA repels AA, hindering the diffusion of AA to the electrode. Similarly, after hybridization with the target miRNA through base-complementary pairing, the photocurrent is further weakened (curve e). Finally, after the addition of SA, SA, and SH-RNA with biotin produced a biotin-streptavidin specific reaction, which further reduces the photocurrent. The reason for the decrease is that the steric resistance reaction is formed after the modification of SA, preventing AA (electron donor) reaching from the electrode surface.[39] The change in impedance and current demonstrate the successful preparation of biosensor.

2.4. Optimization of PEC Biosensor Testing Conditions

The effects of laser wavelength on the photocurrent response of biosensor were investigated with about 405, 450, 532, 660, and 780 nm lasers irradiations (**Figure 4**A) under the laser power of 50 mW and incident angle of 45°. The maximum current is obtained at 450 nm laser irradiation, so this wavelength of laser is selected as the optimal light source. Under the wavelength of 450 nm and incident angle of 45°, the intensity of incident laser was used as a variable. When the incident laser intensity is 80 and 100 mW, the current changes little, as shown in Figure 4B. The prolonged irradiation of the laser with high power will damage the electrode, so 80 mW is the best laser intensity. Effects of different incident angles on current were estimated under wavelength of 450 nm and laser power of 80 mW, which is attributed to that the incident laser needs to pass through plexiglass and solution to reach the electrode. When the incident angles are 0° and 90°, there is almost no current, which may be because that the solution causes the attenuation of the light intensity and no laser hits the front surface of the electrode. The results show that when the incident angle is 60°, the current is the maximum (Figure 4C). Altogether, the excitation laser with the wavelength, power, and incident angle of 450 nm, 80 mW, and 60°, respectively, is chosen as illuminant for miRNA detection.

The schematic diagram of the detection mechanism is shown in Figure 4D. AuNPs/MoS_2/AAO material with excellent photoelectric conversion efficiency is used as the working electrode, in which AuNPs can improve the photogenerated electron capability of MoS_2 and extend the recombination time of electron-hole pairs.[40] After hybridization of the target miRNA-155 with SH-RNA containing biotin, SA can specifically bind to SH-RNA via avidin-biotin interactions, forming macromolecular groups on the SA/miRNA/MCH/SH-RNA/AuNPs/MoS_2/AAO electrode. The macromolecular groups cause steric resistance reactions and impede electrons from AA to the electrode surface, achieving signal amplification. Meanwhile, macromolecular groups can block up the nanochannels making ion transport more difficult. Therefore, the addition of AA can cause a significant change in the current for the detection of

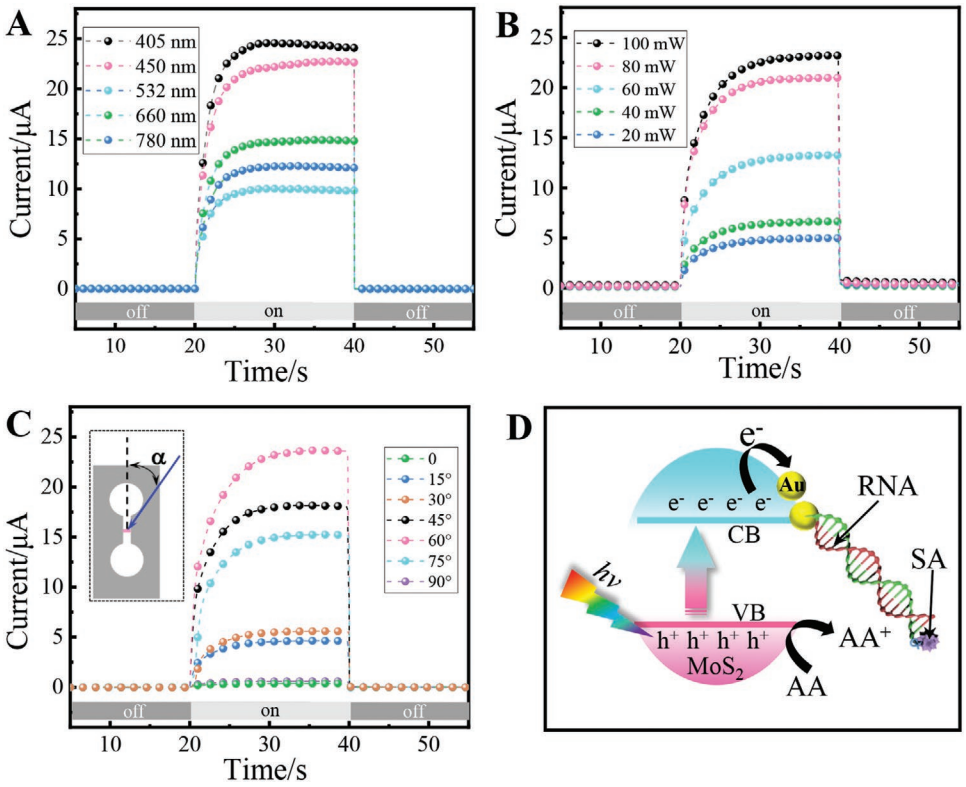

Figure 4. Effects of the A) wavelength, B) intensity, and C) angle of incidence of the irradiated laser on current. The inset in (C) representing the top view of the detection device, and α indicating the incidence angle of the laser. D) Schematic diagram of the photocurrent generation mechanism of the biosensor.

ultra-low concentrations of miRNA-155, which contributes to the enhancement of detection limit. The coupling effects of photocurrent and ionnanochannel current improve the detection sensitivity.

2.5. Ultrasensitive miRNA-155 Detection

Under the optimized conditions, the relationship between the photocurrent and miRNA-155 concentration was studied. The concentrations of miRNA-155 were measured under 10^{-10}, 10^{-11}, 10^{-12}, 10^{-13}, 10^{-14}, 10^{-15}, 10^{-16}, and 10^{-17} M, respectively. As shown in **Figure 5**A, when the miRNA-155 concentration is between 10^{-17} and 10^{-12} M, the current of the biosensor based on AAO with 100 nm nanochannel decreases rapidly with increasing concentration. However, when the concentration exceeds 10^{-12} M, the change of current is no longer obvious. This is because AAO-100 has a larger surface area to adsorb biomolecules with poor conductivity, and smaller nanochannels are more likely to be blocked by biomolecules, affecting ion transport. For AAO-150 (Figure 5B) and AAO-250 (Figure 5C), the current increased as the miRNA-155 concentration increased due to the decline in conductivity. As shown in Figure 5D, the logarithm value of the miRNA-155 concentration is linearly related to the current for PEC biosensor based on AAO-150 within the range of 0.01 fM–0.01 nM. The linear regression equation is I (μA) = −2.77log(c/M)−24.57, and the detection limit is 3 aM (S/N = 3). The linear equation of the PEC sensor based on AA-250 is I (μA) =−3.23log(c/M)−28.26, and the detection limit is 0.02 fM (S/N=3). Although detection limit of the biosensor based on AAO-100 is 8 aM (S/N = 3), which is not far behind AAO-150, it only exhibits a good linear relationship between 10^{-16} and 10^{-12} M. Therefore, the comprehensive detection performance of biosensor based on AAO-150 is better than that based on AAO-100 or AAO-250.

As shown in Figure 5E, the biosensors based on AAO with different nanochannel sizes have diverse detection performance mainly caused by three aspects. 1) As the size of the AAO nanochannel increases, the effective area making for depositing MoS_2 will relatively decrease. The reduction of MoS_2 on surface leads to the decline of photogenerated current. 2) Fewer biomolecules can be combined with AAO/MoS_2 as reduction of MoS_2 during the manufacturing process of the biosensor, which hinders the contact between the AA (electron donor) and the electrode surface. Therefore, AAO with too large size is not conducive to detection. 3) The decrease of nanochannel size causes the deterioration of ion transmission performance, and the biomolecules bound to the channel surface strengthens this effect. In summary, the oversized and undersized AAO nanochannels are not propitious to detection. The PEC biosensor based on AAO-150 has the lowest detection limit in this work, which is favorable for miRNA-155 detection.

In order to test the specificity of the prepared biosensor for detecting microRNA-155, that is, the ability to distinguish between base mismatch sequences. The SH-RNA/Au/MoS_2/AAO with complementary, base non-complementary, and three-base non-complementary miRNA at a concentration of 1 fM were compared. The Current change ($\Delta I = I_1 - I_2$, where I_1 and I_2 are the photocurrent values measured in SH-RNA/MoS_2/AAO, and SA/miRNA/SH-RNA/AuNPs/MoS_2/AAO,

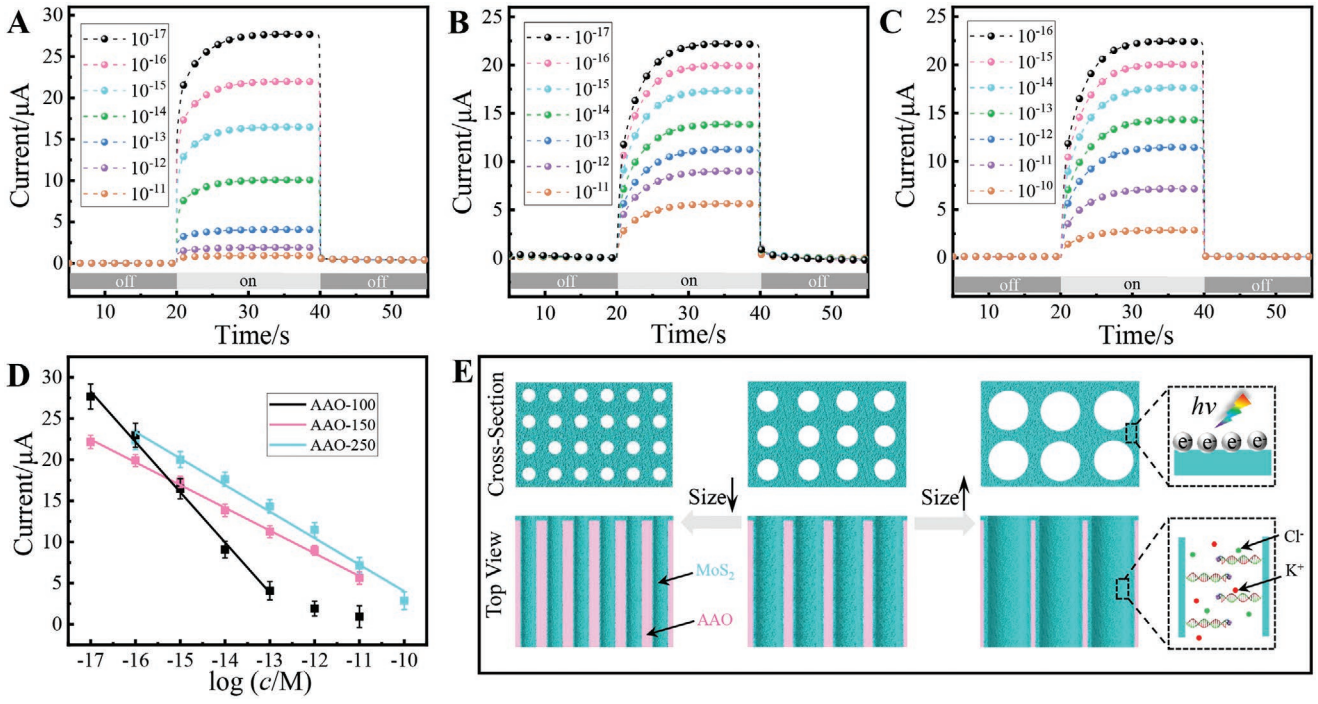

Figure 5. Current response of the PEC biosensor based on A) AAO-100, B) AAO-150, and C) AAO-250 to different concentrations of miRNA-155. D) Calibration curve of current versus logarithm of miRNA-155 concentration. Error bars represent the standard deviation of quintuplicate measurements. E) The mechanism of the PEC biosensor based on AAO with different nanochannel sizes.

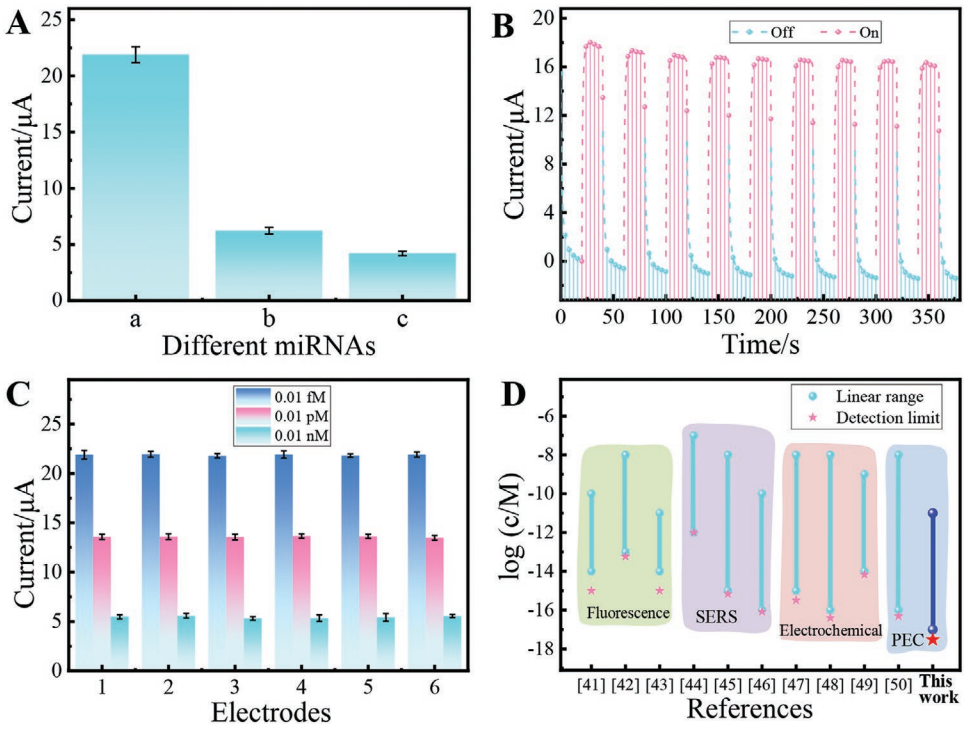

Figure 6. A) The selectivity of the sensing platform hybridized to 0.01 fM miRNA-155 (a), single-base mismatch miRNA (b), and miRNA-21(c). B) Time-based current response of the biosensor. C) Current responses of six equally prepared electrodes for 0.01 fM, 0.01 pM, and 0.01 nM miRNA-155 detections. The Error bars = SD ($n = 4$). D) Comparison of various methods in the references for the detection of miRNA.

respectively.) is counted. It can be seen from **Figure 6**A that ΔI decreases as the degree of base complementation between the miRNA and the probe gradually decreases, indicating that only the complementary strand can form a stable and effective double strand with the probe. The relative standard deviations (RSD) for miRNA-155, single-base mismatch miRNA, and miRNA-21 are 3.24%, 4.82%, and 4.76%, respectively, which indicates that the sensor has excellent specificity.

During the determination of 400 s, current responses of 10 repeated on/off light cycles are recorded. Figure 6B shows that the photocurrent response of the biosensor has no significant change. Figure 6C shows the current obtained by the six independent PEC biosensors constructed to detect the target miRNA at 0.01 fM, 0.01 pM, and 0.01 nM, respectively. The current responses of six equally prepared electrodes have little difference, and the RSD of 0.01 fM, 0.01 pM, and 0.01 nM miRNA-155 are 1.96%, 2.14%, and 6.83%, respectively, which proves that the biosensor could be repeated. Figure 6D and Table S1, Supporting Information, compare the detection linear range and detection limit of the biosensor with other methods.[41–50] The detection device in this paper has a splendid linear range and a lower detection limit, which is better than the previous research. Table S2, Supporting Information, shows the practical application of miRNA-155 detection. 1 pM, 10 fM, and 0.1 fM of miRNA-155 added to the human serum, respectively, are conducted using this detection strategy. The recoveries are 92.5%, 94.2%, and 104.8%, respectively, and the RSDs are no more than 4%, indicating that the biosensor could be used for the detection of miRNA-155 in actual samples.

3. Conclusion

In summary, a novel PEC biosensor for miRNA-155 ultrasensitive detection has been successfully developed based on combining the MoS_2/AAO nanochannel, which can not only generate photoexcitation current as a photoelectric heterojunction semiconductor but also generate ion current as ion transport channels. The synergistic effect of dual currents is beneficial to amplify the detection signal. Under the optimal parameters, the nanochannels diameter of AAO is 150 nm, and the cycles number of ALD-MoS_2 is 70, the ultrasensitive detection limit of the sensor for miRNA-155 is 3 aM. The application of ALD technology to manufacture semiconductor photoresponsive nanochannel has determinate promotion significance. At the same time, the strategy of combining ordinary PEC biosensors with nanochannel provides a new direction for improving the detection property of the biosensor, which deserves attention.

4. Experimental Section

Materials: AAO templates with a thickness of about 100 μm, the pore diameter of about 100, 150, 200, and 250 nm, and an area of 7 mm × 8 mm were obtained commercially (Puyuan Nano, China). Molybdenum chloride ($MoCl_5$), potassium chloride (KCl), 6-mercaptohexanol (MCH), streptavidin (SA), ascorbic acid (AA), and potassium hexacyanoferrate(III) ($K_3Fe(CN)_6$, ≥99.5%) were purchased from Sigma-Aldrich (Shanghai, China). Disodium hydrogen phosphate (Na_2HPO_4, ≥99.0%) and sodium dihydrogen phosphate dehydrate ($NaH_2PO_4{\cdot}2H_2O$, ≥99.0%) were purchased from Sinopharm Chemical

Reagent Co., Ltd. (Shanghai, China). The phosphate buffer solution (PBS) was prepared by mixing a stock solution of 0.1 M NaH_2PO_4 and 0.1 M Na_2HPO_4 and adjusting the pH value. Hydrogen sulfide (H_2S), oxygen (O_2), and nitrogen (N_2) were supplied by Nanjing Special Gas Co. Ltd. (Nanjing, China). The oligonucleotimde sequences were provided by Sangon Biotech Co. Ltd. (Shanghai, China) and their sequences were as follows:Probe SH-miRNA: 5′-SH-ACC CCU AUC ACG AUU AGC AUU AA-biotin-3′. MiRNA-155: 5′-UUA AUG CUA AUC GUG AUA GGG GU-3′. Single-base mismatch: 5′-UUA AGG CUA AUC GUG AUA GGG GU-3′. MiRNA-21: 5′-UAG CUU AUC AGA CUG AUG UUG A-3′.

Preparation of Photoresponsive Nanochannel: As shown in Figure 1A, MoS_2 thin films were deposited on four types of AAO substrates using $MoCl_5$ and H_2S as precursors in commercial ALD equipment (SUNALETMR-100, PICOSUN, Finland). The time of O_2 plasma cleaning was increased to 10 min to make MoS_2 easier to grow on AAO. More details about the controlled growth of MoS_2 using ALD can be found in the team's previous reports.[51,52]

Techniques: An evaporative coating machine (GSL-1800X-ZF4, Kejing, China) was used to form AuNPs at a deposition rate of 0.02 nm s^{-1} and time of 10 min. Electrochemical measurements were performed on an electrochemical workstation (CHI660E, Chenhua Instruments, China) with a conventional three-electrode system. Five lasers (wavelength are 405, 450, 532, 660, and 780 nm, respectively) with adjustable power were used as a source of excitation light. XRD (Smartlab-3, Rigaku, USA) was carried out using Cu Kα radiation ($\lambda = 1.54$ Å) at 35 mA and 50 kV. A transmission electron microscope (TEM, G220, FEI) and a scanning electron microscope (SEM, Inspect F50, FEI) were used for microscopic observations. In the EIS measurements, the receiving cell was filled with 0.1 M KCl solution, and the feeding cell was filled with 0.1 M KCl solution containing 5.0 mM $[Fe(CN)_6]^{3-/4-}$ from 100 kHz to 0.1 Hz. In the PEC measurements, the receiving cell was filled with 0.1 M KCl solution, and the feeding cell was filled with 0.1 M PBS (pH 7.4) contained 0.1 M AA and 0.1 M KCl, and the applied voltage was 0.1 V.

Supporting Information

Supporting Information is available from the Wiley Online Library or from the author.

Acknowledgements

S.J. and L.L. contributed equally to this work. This work is financially supported by the National Natural Science Foundation of China (51822501), the Natural Science Funds for Distinguished Young Scholar of Jiangsu Province (BK20170023), the Fundamental Research Funds for the Central Universities (3202006301, 3202006403), the Qing Lan Project of Jiangsu Province, the International Foundation for Science, Stockholm, Sweden, the Organization for the Prohibition of Chemical Weapons, The Hague, Netherlands, through a grant to Lei Liu (F/4736-2), the grants from Top 6 High-Level Talents Program of Jiangsu Province (2017-GDZB-006, Class A), the Natural Science Foundation of Jiangsu Province (BK20181274), the Tribology Science Fund of State Key Laboratory of Tribology (SKLTKF15A11), Open Research Fund of State Key Laboratory of High Performance Complex Manufacturing, Central South University (Kfkt2016-11), Open Research Fund of State Key Laboratory of Fire Science (HZ2017-KF05), and Open Research Fund of State Key Laboratory of solid lubrication (LSL-1607).

Conflict of Interest

The authors declare no conflict of interest.

Keywords

atomic layer deposition, miRNA-155, photoelectrochemical biosensors, photoresponsive nanochannels

Received: February 25, 2020
Revised: April 29, 2020
Published online:

[1] A. Wasfi, F. Awwad, A. I. Ayesh, *Biosens. Bioelectron.* **2018**, *119*, 191.
[2] A. Nehra, S. Ahlawat, K. P. Singh, *Sens. Actuators, B* **2019**, *284*, 595.
[3] P. Guo, J. Huang, Y. Zhao, C. R. Martin, R. N. Zare, M. A. Moses, *Small* **2018**, *14*, 1703493.
[4] W. Liu, D. Lin, A. Pei, Y. Cui, *J. Am. Chem. Soc.* **2016**, *138*, 15443.
[5] M. Queralt-Martín, M. L. López, M. Aguilella-Arzo, V. M. Aguilella, A. Alcaraz, *Nano Lett.* **2018**, *18*, 6604.
[6] A. S. Gargis, B. Cherney, A. B. Conley, H. P. McLaughlin, D. Sue, *Sci. Rep.* **2019**, *9*, 13501.
[7] R. Bowden, R. W. Davies, A. Heger, A. T. Pagnamenta, M. de Cesare, L. E. Oikkonen, D. Parkes, C. Freeman, F. Dhalla, S. Y. Patel, N. Popitsch, C. L. C. Ip, H. E. Roberts, S. Salatino, H. Lockstone, G. Lunter, J. C. Taylor, D. Buck, M. A. Simpson, P. Donnelly, *Nat. Commun.* **2019**, *10*, 1869.
[8] S. Cho, D. Jang, H. Kang, H. Koh, J. Choi, H. Jung, *Anal. Chem.* **2019**, *91*, 14268.
[9] L. Lu, L. Zhou, J. Chen, F. Yan, J. Liu, X. Dong, F. Xi, P. Chen, *ACS Nano* **2018**, *12*, 12673.
[10] Y. Sun, J. Ma, F. Zhang, F. Zhu, Y. Mei, L. Liu, D. Tian, H. Li, *Nat. Commun.* **2017**, *8*, 260.
[11] Y. Liu, Y. Kong, X. Fan, J. Zhai, L. Jiang, *J. Mater. Chem. A* **2017**, *5*, 19220.
[12] K. Xiao, X. Kong, Z. Zhang, G. Xie, L. Wen, L. Jiang, *J. Photochem. Photobiol., C* **2016**, *26*, 31.
[13] D. Zhang, S. Zhou, Y. Liu, X. Fan, M. Zhang, J. Zhai, L. Jiang, *ACS Nano* **2018**, *12*, 11169.
[14] B. I. Karawdeniya, Y. M. N. D. Bandara, J. W. Nichols, R. B. Chevalier, J. R. Dwyer, *Nat. Commun.* **2018**, *9*, 3278.
[15] R. Nouri, Z. Tang, W. Guan, *ACS Sens.* **2019**, *4*, 3007.
[16] Y. Ying, Y. Li, J. Mei, R. Gao, Y. Hu, Y. Long, H. Tian, *Nat. Commun.* **2018**, *9*, 3657.
[17] C. Liu, E. I. Gillette, X. Chen, A. J. Pearse, A. C. Kozen, M. A. Schroeder, K. E. Gregorczyk, S. B. Lee, G. W. Rubloff, *Nat. Nanotechnol.* **2014**, *9*, 1031.
[18] M. Shankla, A. Aksimentiev, *Nat. Nanotechnol.* **2019**, *14*, 858.
[19] Y. Li, G. Du, G. Mao, J. Guo, J. Zhao, R. Wu, W. Liu, *ACS Appl. Mater. Interfaces* **2019**, *11*, 38055.
[20] F. D. Guzel, H. Avci, *IEEE Sens. J.* **2018**, *18*, 2641.
[21] C. Liu, N. Kim, G. W. Rubloff, S. B. Lee, *Nanoscale* **2017**, *9*, 11566.
[22] T. S. Walmsley, B. Chamlagain, U. Rijal, T. Wang, Z. Zhou, Y. Q. Xu, *Adv. Opt. Mater.* **2019**, *7*, 1800832.
[23] M. Long, P. Wang, H. Fang, W. Hu, *Adv. Funct. Mater.* **2019**, *29*, 1803807.
[24] W. Hong, G. W. Shim, S. Y. Yang, D. Y. Jung, S. Y. Choi, *Adv. Funct. Mater.* **2019**, *29*, 1807550.
[25] P. M. Campbell, C. J. Perini, J. Chiu, A. Gupta, H. S. Ray, H. Chen, K. Wenzel, E. Snyder, B. K. Wagner, J. Ready, E. M. Vogel, *2D Mater.* **2018**, *5*, 015005.
[26] W. Zhao, J. Xu, H. Chen, *Chem. Rev.* **2014**, *114*, 7421.
[27] P. Li, X. Liu, C. Mao, B. Jin, J. Zhu, *Anal. Chim. Acta* **2019**, *1048*, 42.
[28] S. Wu, H. Huang, M. Shang, C. Du, Y. Wu, W. Song, *Biosens. Bioelectron.* **2017**, *92*, 646.
[29] M. Wang, H. Yin, Y. Zhou, C. Sui, Y. Wang, X. Meng, G. I. N. Waterhouse, S. Ai, *Biosens. Bioelectron.* **2019**, *128*, 137.
[30] Y. Chen, S. Zhang, H. Dai, Z. Hong, Y. Lin, *Biosens. Bioelectron.* **2020**, *148*, 111809.

[31] J. Zhang, A. Yang, X. Wu, J. van de Groep, P. Tang, S. Li, B. Liu, F. Shi, J. Wan, Q. Li, Y. Sun, Z. Lu, X. Zheng, G. Zhou, C. Wu, S. Zhang, M. L. Brongersma, J. Li, Y. Cui, *Nat. Commun.* **2018**, *9*, 5289.
[32] L. Fei, S. Lei, W. Zhang, W. Lu, Z. Lin, C. H. Lam, Y. Chai, Y. Wang, *Nat. Commun.* **2016**, *7*, 12206.
[33] J. Benson, M. Li, S. Wang, P. Wang, P. Papakonstantinou, *ACS Appl. Mater. Interfaces* **2015**, *7*, 14113.
[34] X. Fan, P. Xu, D. Zhou, Y. Sun, Y. Li, M. Nguyen, M. Terrones, T. Mallouk, *Nano Lett.* **2015**, *15*, 5956.
[35] A. Sharma, M. A. Verheijen, L. Wu, S. Karwal, V. Vandalon, H. C. M. Knoops, *Nanoscale* **2018**, *10*, 8615.
[36] M. Wang, H. Yin, N. Shen, Z. Xu, B. Sun, S. Ai, *Biosens. Bioelectron.* **2014**, *53*, 232.
[37] Y. Liu, Y. Huang, X. Duan, *Nature* **2019**, *567*, 323.
[38] X. Li, Y. Fang, S. Q. Wu, Z. Z. Zhu, *AIP Adv.* **2015**, *5*, 057143.
[39] N. Fu, Y. Hu, S. Shi, S. Ren, W. Liu, S. Su, B. Zhao, L. Weng, L. Wang, *Analyst* **2018**, *143*, 1705.
[40] Y. Shi, J. Wang, C. Wang, T. Zhai, W. Bao, J. Xu, X. Xia, H. Chen, *J. Am. Chem. Soc.* **2015**, *137*, 7365.
[41] C. Hong, X. Chen, J. Li, J. Chen, G. Chen, H. Yang, *Chem. Commun.* **2014**, *50*, 3292.
[42] L. Wang, R. Deng, J. Li, *Chem. Sci.* **2015**, *6*, 6777.
[43] M. Xiao, A. R. Chandrasekaran, W. Ji, F. Li, Q. Li, L. Li, *ACS Appl. Mater. Interfaces* **2018**, *10*, 35794.
[44] L. Qi, M. Xiao, X. Wang, C. Wang, L. Wang, S. Song, *Anal. Chem.* **2017**, *89*, 9850.
[45] X. Yang, S. Wang, Y. Wang, Y. He, Y. Chai, R. Yuan, *ACS Appl. Mater. Interfaces* **2018**, *10*, 12491.
[46] Y. He, X. Yang, R. Yuan, Y. Chai, *Anal. Chem.* **2017**, *89*, 8538.
[47] L. Liu, S. Zhu, Y. Wei, X. Liu, S. Jiao, J. Yang, *Biosens. Bioelectron.* **2019**, *144*, 111660.
[48] S. Xu, Y. Chang, Z. Wu, Y. Li, R. Yuan, Y. Chai, *Biosens. Bioelectron.* **2020**, *149*, 111848.
[49] Z. Cao, F. Duan, X. Huang, Y. Liu, N. Zhou, L. Xia, Z. Zhang, M. Du, *Anal. Chim. Acta* **2019**, *1082*, 176.
[50] L. Meng, Y. Li, R. Yang, X. Zhang, C. Du, J. Chen, *Chem. Commun.* **2019**, *55*, 2182.
[51] Y. Huang, L. Liu, J. Yang, Y. Chen, *Langmuir* **2019**, *35*, 3651.
[52] J. Yang, L. Liu, *ACS Appl. Mater. Interfaces* **2019**, *11*, 36270.